Initial Results of the TUBIN Small Satellite Mission for Wildfire Detection

Julian Bartholomäus[a,*], Merlin F. Barschke[a,b], Philipp Werner[a], Enrico Stoll[a]

[a]*Technische Universität Berlin, Chair of Space Technology, Straße des 17. Juni 135, 10623 Berlin, Germany*
[b]*Deutsches Elektronen-Synchrotron DESY, Platanenallee 6, 15738 Zeuthen, Germany*

Abstract

TUBIN is a microsatellite mission tasked with the demonstration of microbolometer technology for the detection of high-temperature events. To this end, the spacecraft employs a set of two microbolometers sensitive in the thermal range of the electromagnetic spectrum as well as a complementary CMOS-based imager for the visible spectrum. Additionally, the mission serves to demonstrate the upgraded capabilities of the TUBiX20 microsatellite platform after its initial implementation within the TechnoSat mission, launched in 2017. Therefore, the platform was upgraded with star trackers for enhanced attitude determination to enable the pointing accuracy required by the mission. Launched in June 2021, TUBIN has already successfully detected wildfires and volcanic activity in different biomes across the globe. Additionally, the sensor suite of the TUBIN mission was applied to examine its capabilities in the assessment of light-pollution in dedicated night time imaging campaigns. In this paper, we present and analyze data sets captured in the first six months of operation to illustrate capabilities, accomplishments, and challenges regarding payload operation, calibration, and data analysis for the TUBIN mission. Finally, the plans for the second half of TUBIN's nominal lifetime are outlined, including an on-orbit calibration campaign and increased automation in payload operations.

Keywords: orbit results, small satellite, wildfire, microbolometer, remote sensing, thermal infrared

1. Introduction

The global average temperature has risen dramatically during the past decades and is predicted to further rise within the following years [1, 2]. This development is expected to increase the likelihood of extreme weather phenomena such as droughts, storms and wildfires, causing significant ecological and economical damage. Extended wildfire seasons are also fueling this development due to the emission of greenhouse gases into the atmosphere [3].

The detection of high-temperature events from space offers a high coverage with fixed costs. Amongst present satellites with fire detection capabilities are conventional satellites such as Terra and Aqua and the Landsat-series but also smaller satellites already operational or in preparation [4]. Since smaller satellites have become increasingly popular not only for education or technology demonstration but also for challenging applications in and beyond Earth's orbit, suitable instrumentation for the detection of high-temperature events along with on-orbit processing capabilities are a focal point of the research [5, 6].

Microbolometers are sensitive in the thermal range of the electromagnetic spectrum and are a suitable option for small satellite systems since they do not require active cooling. The TUBIN mission employs two microbolometers to demonstrate and further investigate their use for detecting high-temperature events from orbit.

The TUBIN spacecraft, launched into low-Earth orbit on June, 30th 2021, is based on the TUBiX20 platform of the chair of space technology at Technische Universität Berlin. The TUBiX20 platform is designed to support missions with a launch mass of up to 50 kg and was first demonstrated within the TechnoSat mission which carried several novel small satellite components [7, 8].

Technische Universität Berlin possesses a heritage of more than 30 years in the development and operation of small satellites, having launched a total of 27 satellites to date, 19 of which are still being operated. Thus, relevant expertise could be established within key disciplines in the context of space missions, such as mission

*Corresponding author

Email addresses: `julian.bartholomaeus@tu-berlin.de` (Julian Bartholomäus), `merlin.barschke@tu-berlin.de` (Merlin F. Barschke), `philipp.werner@tu-berlin.de` (Philipp Werner), `e.stoll@tu-berlin.de` (Enrico Stoll)

operations and ground infrastructure [9], structural and thermal design [10, 11], attitude determination and control systems [12], onboard software [13], and ground support systems [14].

In this paper, we present orbit results of the first six months of the TUBIN mission with a focus on the preliminary results generated throughout the commissioning of the payload.

2. The TUBIN Mission

The TUBIN mission is tasked with the demonstration of microbolometer technology for the detection of high-temperature events. While peak reflectances of typical forest fire temperatures lie within the medium-wavelength infrared (MWIR) range ([15]), high-temperature events remain detectable within the thermal infrared (TIR) range that the TUBIN infrared imagers are sensitive to. MWIR sensors typically require active cooling and, thus, result in a higher overall complexity of the spacecraft. Conventional spacecraft used for fire detection employ detectors sensitive in both the MWIR and the TIR range, respectively. For a classification of TUBIN in the context of space-systems with fire detection capabilities, the reader is referred to [4].

Additionally, TUBIN demonstrates an upgrade of the modular TUBiX20 microsatellite platform regarding its attitude determination capabilities in order to enable the platform to support demanding Earth observation missions [16]. As a secondary objective, TUBIN is tasked with demonstrating payload data processing for the preselection of imagery aboard the spacecraft. A digital rendering of the TUBIN spacecraft is shown in Figure 1.

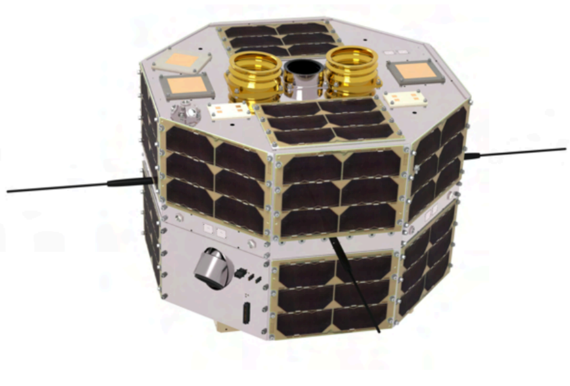

Figure 1: Digital rendering of the TUBIN satellite in flight configuration [4]. At the upper side of the spacecraft, which is nominally pointing towards nadir during operations, the baffles of the two infrared microbolometers and the visible spectrum camera can be seen.

Table 1: Overview of the main parameters and features of the TUBIN mission and spacecraft.

Payloads	2 TIR and 1 VIS imagers, X-band transceiver
Orbit	530 km SSO
Launch Date	June 30th, 2021
Design Lifetime	1 year
Spacecraft mass	22.6 kg
Spacecraft volume	$465 \times 465 \times 305\,mm^3$ (without antennas and baffles)
TM/TC link	UHF, telemetry in S band and (experimental) in X band
Payload data downlink	S band and (experimental) X band
Attitude sensors	Star trackers, fibre optic rate sensors, Sun sensors, IC and fluxgate magnetometers, MEMS gyroscopes
Position sensors	GPS receiver, retro-reflectors
Attitude actuators	Magnetorquers, reaction wheels

The TUBIN spacecraft employs a payload consisting of two thermal infrared (TIR) Vanadium oxide (VOx) microbolometer focal plane arrays sensitive in the thermal infrared range of the electromagnetic spectrum as well as a CMOS-based sensor sensitive in the visible spectrum (VIS) to assist in the geolocation of wildfires. Furthermore, TUBIN carries a novel X-band transceiver supporting downlink in X band and uplink in S band and X band. Enabling a high-speed data downlink of up to 56 Mb/s, this payload complements the Earth observation tasks of TUBIN [17]. The main parameters of the TUBIN mission are listed in Table 1.

2.1. The TUBIN spacecraft

The overall systems overview of the TUBIN spacecraft follows the TUBiX20 architecture and expands on the foundation established within the TechnoSat mission. Supplementary to the Controller Area Network (CAN) bus that is implemented as main data bus between the distributed system of computational nodes, a payload data interface in the form of an Ethernet hub has been installed that interconnects the payloads with the platform's payload data handling (PDH) node. Additionally, the attitude determination and control system has been upgraded significantly by the addition of two star trackers and a pair of fluxgate magnetometers. The star trackers are aligned at an angle of 90° to one another and operated simultaneously to provide high-precision attitude data of the spacecraft during nominal payload operations. In order to improve the accuracy in position knowledge, a GPS receiver was added to the satellite and the arrangement of the laser retro reflectors was improved.

The systems overview of the TUBIN satellite is illustrated in Figure 2. Here, dark blue tiles denote TUBiX20 nodes that interface to the platform's common power (red) and data buses (blue). These nodes serve as interfaces to control units such as sensors or

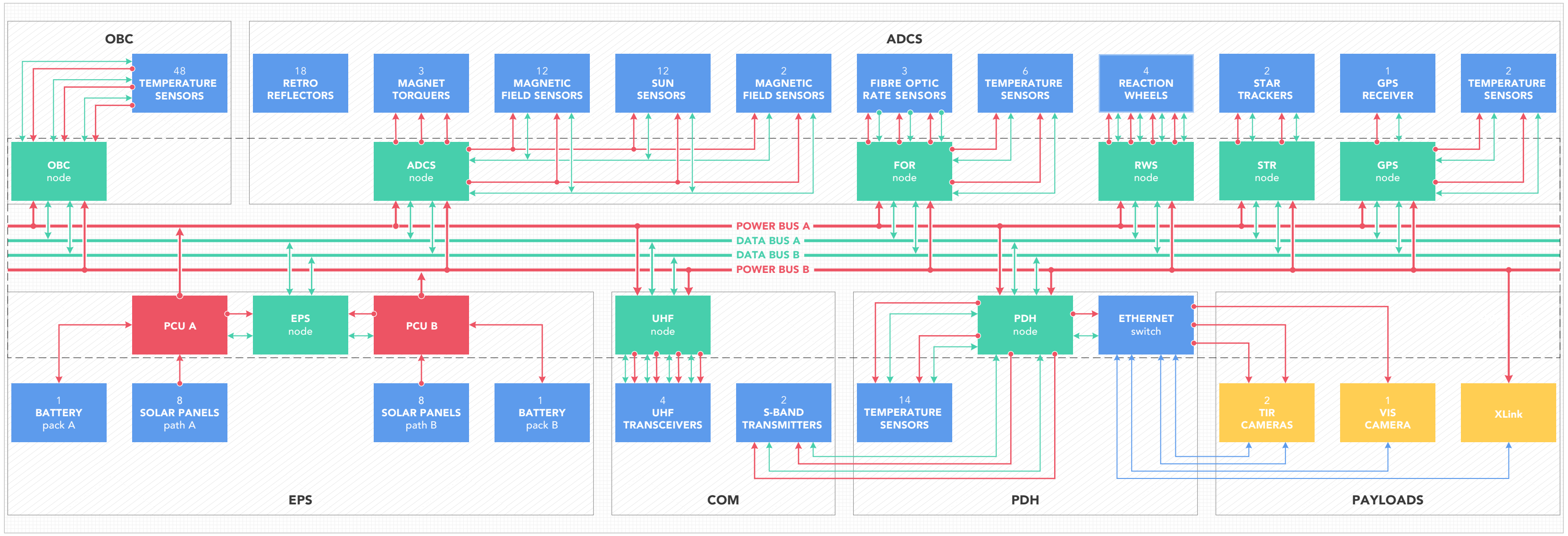

Figure 2: Systems overview of the TUBIN spacecraft. In the center of the image the platform's central power (red) and data (blue) buses are shown, that interconnect the TUBiX20 nodes (dark blue). The nodes provide the interface to control units such as sensors or actuators, that are depicted in light blue. All nodes are implemented cold redundantly except for the EPS node that operates in warm redundancy and manages the redundancies of all other nodes. Interconnections of the payload data bus are shown in green (Figure adapted from [16]).

actuators (denoted by light blue tiles) and process and distribute their data. The payload data bus interconnecting payloads and platform is depicted in green. All nodes are implemented in cold redundancy to increase the robustness of the system. An exception is the electrical power system (EPS) node that is operated in warm redundancy and controls the redundancy of all other nodes. For a more detailed description of the TUBiX20 platform and the TUBIN spacecraft the reader is referred to [18] and [16], respectively.

2.2. *The TUBIN payload*

Continuing its modular development approach also within the design of the payload, each camera implements an electronics stack that consists of the same three types of printed circuit boards (PCBs):

1. the interface board implements the Ethernet phy that enables communication between the satellite platform and payloads,
2. the processing unit, that is identical in all three cameras and hosts a powerful processor capable of performing image processing directly on the camera itself, and
3. the power unit that is tasked with providing all necessary power levels to supply the sensor head board and processing unit.

Finally, the sensor head board, that may be an assembly of several elements, implements the sensors for the different spectral ranges.

This approach allows to easily configure the electronics stack to support different types of sensors. Data can be interchanged between cameras and delivered to the X-band transceiver for downlink via Ethernet. Furthermore, payload data and telemetry may also be sent to the payload data handling (PDH) node for transmission via the platform's S-band transmitters or from the PDH onwards over the central data bus to the on-board computer (OBC) node and subsequent transmission via ultra-high frequency (UHF) band.

The imagers of the TUBIN payload assembly are arranged such that their field of view interleaves in the centre of the VIS imager. As such, the entire width of the TIR imagers is covered by the VIS camera, improving the georeferencing of features within both TIR and VIS images. About 50 % of each TIR scene lies within both TIR imagers enabling the examination of noise reduction and cross calibration (cf. Figure 3).

All three TUBIN payload imagers are fixed frame arrays based on commercial off-the-shelf (COTS) components. No mechanical shutters are implemented to

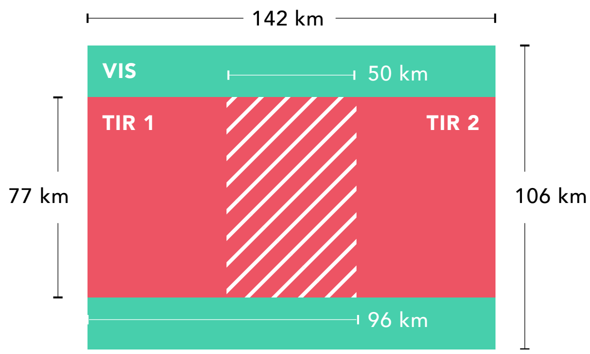

Figure 3: Ground projection of the field of view (FOV) of the three payload cameras of TUBIN in nadir pointing. Both TIR microbolometers combined cover the same width and share approximately 50 % of their respective FOVs (Figure adapted from [16]).

Table 2: Main parameters of the two camera types, i.e. thermal infrared (TIR) and visible light spectrum (VIS), that constitute the TUBIN imaging payload for a 530 km orbit [16].

	Thermal infrared (TIR)	Visible (VIS)
Mass	450 g	240 g
Volume	$162 \times 83 \times 76$ mm^3	$135 \times 64 \times 64$ mm^3
Sensor technology	VOx microbolometer	CMOS
Optics	Fixed focus GeAs lens	Fixed focus and NIR filter
Pixel pitch	17 µm	1.67 µm
Frame format	640×512 pixels	3664×2748 pixels
GSD	150 m	39 m
Mounting angle	±2.43°	0°
Swath (combined)	96 km (142 km)	142 km
Focal length	60 mm	22.9 mm
f-number	1.25	1.4
Power consumption	4 W	3 W

avoid mechanical failures. The main parameters of the TUBIN payload are summarised in Table 2. The payload assembly in flight configuration and without the baffles that are attached to the top deck of the satellite (cf. Figure 1) is shown in Figure 4.

Next to the microbolometer sensors sensitive to radiation in the thermal infrared range of the electromagnetic spectrum, TUBIN also features a camera sensitive to visible light. This camera is based on a CMOS sensor and implements a fixed focus lens with a near-infrared cut-out filter. It is mainly operated at two different resolutions, 38.65 m ground sample distance (GSD) full resolution and 154.6 m GSD reduced resolution resulting in frame formats of 3468×2748 pixels and 912×688 pixels, respectively. The latter format is created by binning across pixels with the same Bayer filter color. The reduced resolution is predominantly used for extended imaging campaigns to reduce the payload data volume that is limited by the downlink capabilities of the platform. The VIS camera is used mainly to assist in the im-

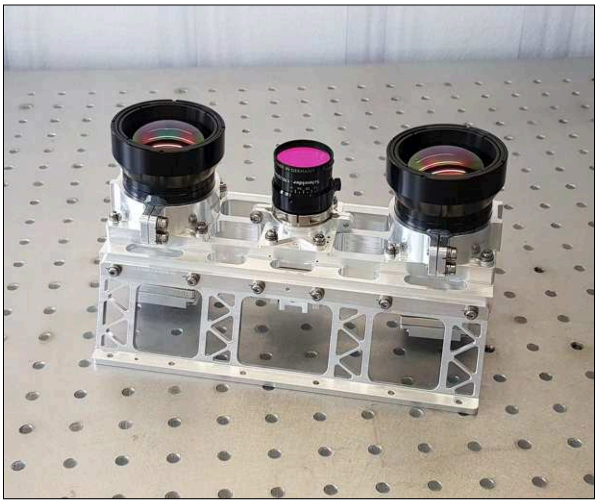

Figure 4: The TUBIN payload assembly in flight configuration. The TIR imagers at the sides and the VIS imager in the center are mounted onto a common optical bench that is attached to the central deck of the spacecraft's three decks.

age registration of the thermal infrared data and thereby improves localisation of wildfires on Earth. Due to its higher spatial resolution when being compared to the TIR imagers, it can detect smaller features and structures within the imagery. Additionally, the camera is also used for estimating the mounting matrices of the payload assembly within the satellite reference frame with high fidelity. Similar experiments have already been used within the TechnoSat mission for the verification of the satellite's attitude determination and control system (ADCS) [7, 19]. Since the VIS camera is capable of detecting stars it can be used as a star camera. The addition of spectral data in the VIS range of the electromagnetic spectrum also supports the detection of clouds within the imagery.

Another application area for the TUBIN payload assembly is the detection of light-pollution which has become a focus of research in recent years [20, 21] and, consequently, the capabilities of the TUBIN VIS camera were investigated in this regard.

2.3. Payload data acquisition and processing

To acquire payload data with the TIR imagers, an operational scenario was defined that includes the collection of the target imagery together with a number of calibration frames. To this end, the TUBIN spacecraft points towards free-space to collect calibration frames that are used when processing the data to account for different pixel offsets before and after the acquisition of TIR data. For a more detailed description of this imaging scenario, the reader is referred to [16]. Collected TIR data is pre-processed using the aforementioned calibration frames and converted to brightness temperatures based on an on-ground calibration campaign performed before launch.

For the purpose of wildfire detection, a fire detection algorithm using simulated data based on the ASTER instrument [22] and the TET-1 spacecraft [23] was developed for the TUBIN mission. It is a multi-stage algorithm based on the brightness temperatures of the scene retrieved from microbolometer data. A detailed description of the fire detection algorithm can be found in [24]. The different steps of the algorithm are:

1. Differentiate between daytime and nighttime imagery. To account for differences in overall scene brightness temperature levels, threshold values and the area examined for local thresholding were determined for daytime and nighttime data individually.
2. Filter for obvious cloud pixels via global threshold. Since the presence of clouds affects the global brightness temperature levels of the scene, they are flagged within an early stage of the algorithm and pixels flagged as clouds are not considered for the remainder of the processing steps.
3. Filter for obvious fire pixels via global threshold. Pixels exhibiting brightness temperatures above a certain threshold value are considered obvious fire pixels. No further processing is required to validate their status as an active fire. Obvious fire pixels are excluded for the remainder of the processing steps.
4. Filter for candidate fire pixels via global threshold. Pixels that exhibit brightness temperature values below the obvious-fire-pixel-threshold and above the candidate-fire-pixel-threshold are flagged as candidate fire pixels. These pixels are examined in a final step to determine whether they contain an active fire.
5. Evaluate candidate fire pixels through local threshold. Here, each candidate pixel is examined individually. If the pixel exhibits a brightness temperature higher than the average of its direct vicinity with an additional threshold, it is confirmed as a fire pixel. Cloud pixels and obvious fire pixels are not considered when determining the local average brightness temperature.

The threshold values were empirically determined using 108 scenes of wildfires and high-temperature events predominantly located in the Western United States. Successfully detected wildfires within the scenes are validated using satellite imagery of other satellite systems with wildfire detection capabilities (cf. [4]). Next to wildfires, there are further high-temperature events that can be monitored using thermal infrared imagers. These events include gas flares [25, 26] and volcanic activity. The value of monitoring volcanic events in the TIR range was, for instance, surveyed in [27] and, thus, the capabilities of the TUBIN payload shall be assessed in this regard.

3. TUBIN mission operations and results

The TUBIN spacecraft was launched into a Sun-synchronous orbit with a height of 530 km on June, 30th 2021 aboard Transporter-2, SpaceX's second dedicated smallsat rideshare mission. Figure 5 shows the integration of TUBIN onto the launch adapter at the launch site in Cape Canaveral.

Figure 5: Integration of the TUBIN spacecraft onto the launch adapter five weeks prior to launch in Cape Canaveral. The remove-before-flight items covering solar cells and star tracker optics are still in place (image credit: EXOLAUNCH).

During the first passes of the ground station in Berlin after separation, the spacecraft was successfully contacted and after a thorough health-check as well as clock and position updates, the satellite's GPS-receiver was activated to assist in the identification of the spacecraft after separation through orbit propagation. Following the commissioning of vital platform components, first-light imagery for VIS and TIR cameras has been collected on July, 6th, just one week after launch.

3.1. Acquisition of the first wildfire

After commissioning of the complete attitude determination and control system (ADCS) was concluded, the first dedicated imaging campaign was conducted on July, 13th over southern Brasil.

Active wildfire targets were chosen from data provided through the Fire Information for Resource Management System (FIRMS). This service distributes active fire data of the VIIRS and MODIS instruments on spacecrafts NOAA-20, Suomi NPP, and Terra and Aqua, within three hours of acquisition.

The MODIS instrument is a spectrometer with moderate spatial resolution that offers a total of 36 bands sensitive between the VIS and the TIR range of the electromagnetic spectrum. A description of the MODIS fire products can be found in [28]. The VIIRS instrument covers the same range in a total of 22 bands. The fire detection capabilities of the VIIRS instrument are detailed in [29].

For the imaging campaign, TUBIN was set to nadir-pointing mode and two consecutive images were captured by all three imagers simultaneously at an interval of 9 s to allow for a continuous swath. Figure 6 shows a combined image composed by the two frames that were captured by TUBIN's TIR2 camera. They feature the *Parque Nacional das Emas* in the south of Goís, Brasil. The satellite imagery was converted to brightness temperature values. Here, lighter pixels represent higher brightness temperature while darker pixels denote lower values. By examining the imagery with the naked eye one can identify a bright spot in the top left corner of the picture and a smaller bright spot towards the centre-right of the scene. These spots were flagged as wildfires by the TUBIN fire detection algorithm and they exhibit a dark feature surrounding them that was assumed to be a smoke plume originating from the seat of fire obstructing the infrared radiation and, thus, leading to a lower apparent brightness temperature of the obstructed pixels.

To verify that the detected features were wildfires, they had to be compared against a reliable and proven data source. To this end, satellite data with fire detection capabilities of the same region that was captured at a similar point in time was used to validate the results. Firstly, MODIS data captured on July, 13th by the Terra satellite was used to locate the wildfires. It could be shown that both wildfires were detected by the MODIS active fire product as well. Figure 7 shows the location of the wildfires within the MODIS scene. Since the reflectance of active wildfires relative to the background is the highest within the medium-wavelength infrared [15], band 20 of the MODIS instrument was chosen in this representation. Here, structure and location is clearly visible within the MWIR data. In agreement with the image data recorded by TUBIN'S TIR imager, the wildfire on the right-hand side of the highlighted-section of the scene is comparatively more dim and features a more extensive smoke plume while the concentrated wildfire on the left-hand side is exhibiting a higher reflectance and appears lighter.

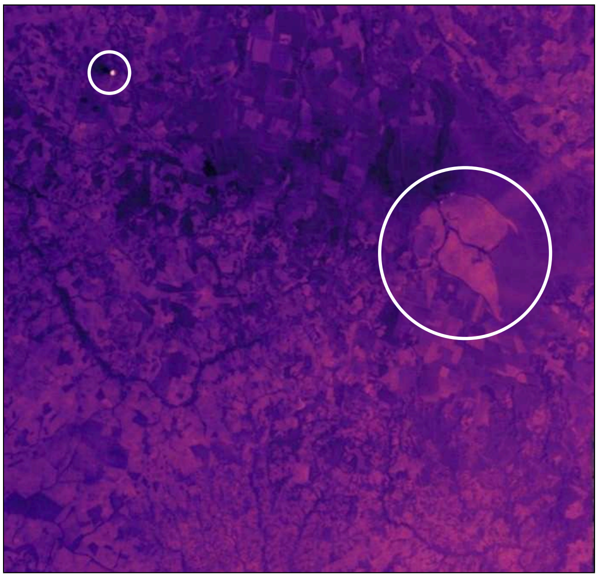

Figure 6: Stitch of two TIR images featuring the first fires detected by the TUBIN spacecraft taken on July, 13th over Brasil at 17:28:30 UTC and 17:28:39 UTC, respectively.

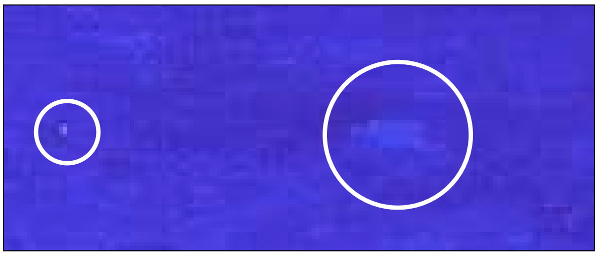

Figure 7: Validation of the location of the first fires detected by TUBIN using a MODIS image granule taken on July, 13th at 17:45:00 UTC. The image shows MODIS Band 20 sensitive in the MWIR range of the electromagnetic spectrum.

Figure 8: Validation of the location of the first fires detected by TUBIN using a VIIRS image granule taken on July, 13th at 18:00:00 UTC. The image shows VIIRS Band I04 sensitive in the MWIR range of the electromagnetic spectrum.

The same procedure was used to validate this specific wildfire with another system, the VIIRS instrument that provides TIR imagery at a higher spatial resolution than MODIS. Figure 8 shows a scene captured on July, 13th by the VIIRS instrument on the NOAA-20 spacecraft. For this representation, band I04 was chosen which is sensitive to radiation in the MWIR range of the electromagnetic spectrum due to its increased relative reflectance of wildfires compared to background pixels in this range. Here, the first wildfire is located at the edge of the scene. Since the VIIRS instrument is a whiskbroom scanner, features located towards the edges of the swath in across-track direction increasingly suffer from bow-tie distortions. Due to bow-tie deletion, some lines were removed from the image granules. Additionally, adjacent scan lines still begin to overlap which explains why the features highlighted in the figure appear on both sides of the deleted lines. A description of the scan geometry and the associated effects can be found in [30]. Nonetheless, the imagery can be used to validate the existence of the high-temperature events present within the TUBIN data. Here, both active wildfires on the left-hand side of the highlighted section are clearly visible but also the small hotspots at the rim of the lighter-coloured area of the national park which is clearly visible in Figure 6, as well.

3.2. *Artifacts within the raw imagery*

Following this first successful acquisition of fire data, the commissioning of payload and spacecraft continued and TIR data of several forest fires in Northern America, Europe and Asia were recorded. The first imaging campaigns of TUBIN were conducted at an experimental level and, thus, did not exercise the entire nominal imaging routine for the acquisition of TIR data. For calibration purposes, the spacecraft nominally points its thermal infrared imagers towards free space before and after the acquisition of TIR payload data for the purpose of calibration. A detailed description of nominal payload operations can be found in [16]. In absence of a mechanical shutter and a calibration source aboard the spacecraft, free space offers a readily available, uniform reference at temperatures below the sensitive range of the infrared imagers which can be used to eliminate fixed-pattern noise within the imagery.

VOx microbolometer arrays are prone to artifacts caused by direct exposure to high irradiation sources such as the Sun. However, these artifacts have been shown to disperse over time [31]. The first testimony of this behaviour was already observable in the first imaging campaign (cf. Figure 6) in the centre-right of the frame stretching towards the centre.

Figure 9 assembles sample frames exhibiting artifacts associated with direct exposure to the Sun. All frames

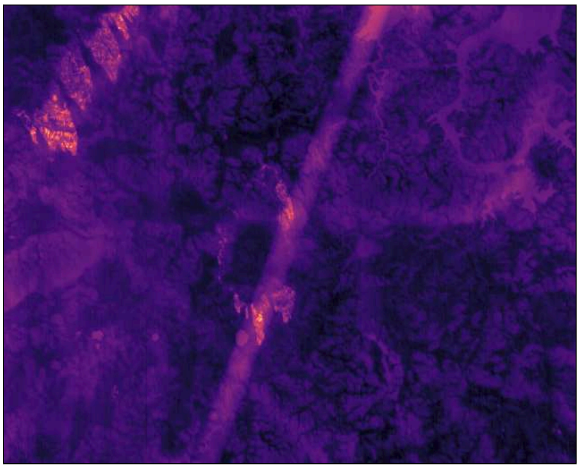

(a) Nighttime TIR imagery of wildfires taken on July, 27th 2021 at 17:33:58 UTC over central Siberia, Russia.

(b) Daytime TIR imagery of wildfires taken on July, 28th 2021 at 06:29:59 UTC over central Siberia, Russia.

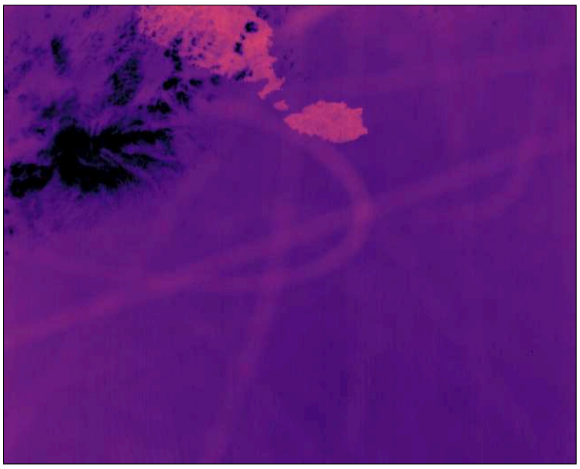

(c) Daytime TIR imagery depicting the coast South of Sicily, Italy taken on August, 3rd 2021 at 13:29:17 UTC.

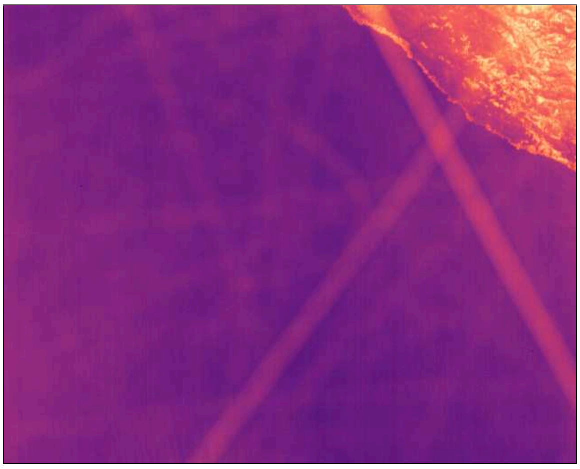

(d) Daytime TIR imagery showing the westcoast of the United States taken on August, 31st 2021 at 22:45:35 UTC.

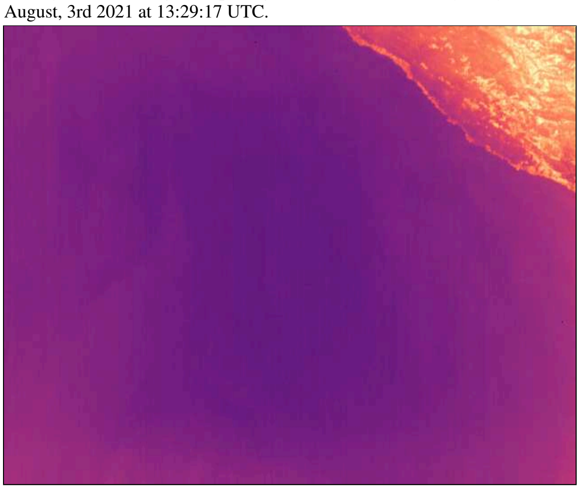

(e) The same scene as portrayed in (d) but corrected using free space imagery taken before and after the imaging campaign.

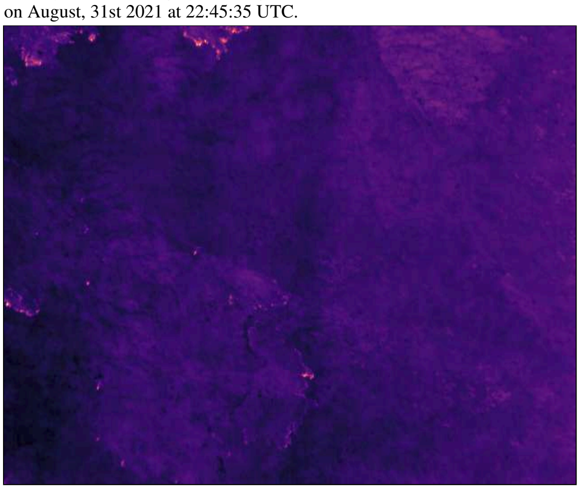

(f) The same scene as portrayed in (b) but corrected using a composite of all 14 scenes of that imaging campaign.

Figure 9: Development of the prevalence of imaging artifacts associated to the TIR imagers being exposed to the Sun. These artifacts can be removed from the imagery using two different approaches, namely based on free-space calibration frames or, with less precision, by the use of several frames depicting the same scene.

highlighted were taken by the TIR2 imager of TUBIN. Subfigure 9a shows a nighttime frame of central Siberia. It suffers from a prominent stripe through the center of the image amongst other less significant offsets. Subfigure 9b shows a daytime image taken approximately 13 hours later in the same region. It features a prominent oval artifact that may have been shaped by the Sun moving through the field-of-view during a manoeuvre of the spacecraft. Since it was not present within 9a, it must have occurred within the 13 hours time frame between the images, which explains why the associated offset is significantly higher than those of the other artifacts visible in the frame. For the given image, the maximum offset introduced by the artifact amounts to as much as 1165 digital numbers (DN) for a 14 bit-quantized image. For the given scenery in 9b, this constitutes an offset of more than 28 % with respect to directly neighboring pixels. Looking at Subfigure 9c, one can see that the formerly prominent artifact is blending in with other artifacts in terms of intensity, indicating that recovery of the pixels to their original offset is non-linear over time. Here, the area with the highest offset is superposed with another imaging artifact and the maximum offset between artifact and unaffected neighbouring pixels constitutes to 282 DN or approximately 6.5 %.

Subfigure 9d shows a scene captured approximately 34 days after the formation of the artifacts. The arch of the oval artifact still remained visible within the uncorrected image. At this stage, the maximum offset amounts to 181 DN or approximately 5.3 %. After the rapid decrease in intensity over the first week, the rate of decrease in pixel offset associated with this artifact appears to have declined. As late as December, more than 4 months after the exposure to the Sun, this artifact has faded completely. Since these artifacts are persistent throughout the imagery and always affect the same pixels in the same way, they can be removed from the imagery. There are two different approaches that have been used for artifact removal from direct Sun exposure in the TUBIN imagery. The first approach to correcting the scenery is illustrated in Subfigure 9e. Here, the scene is corrected by a master dark created from free-space pointing frames taken before and after the imaging campaign. This approach is independent of the number of pictures taken throughout the imaging campaign or its variance, i.e. it is also valid when performing target-pointing manouevres that will only generate images of the same scene. The second approach was, for instance, used for the scene in Subfigure 9b. Assuming a sufficient amount of scenes, data can be corrected by pixel-wise deducting the mean value across all scenes and globally adding the mean value of the frame as not to alter the overall intensity (cf. Eq. 1). Here, i and j denote pixel indices, k denotes the image index and n is the total number of scenes used for the correction of the scene. Variables i_{tot} and j_{tot} denote the number of lines and columns of the infrared sensor array, respectively.

$$DN_{corr,k,i,j} = DN_{k,i,j} - \frac{\sum_{k=1}^{n} DN_{k,i,j}}{n} + \frac{\sum_{k,i,j} DN_{k,i,j}}{n \cdot i_{tot} \cdot j_{tot}} \quad (1)$$

Subfigure 9f shows the scene that was corrected with the scene-based approach. A total of 14 scenes have been captured within this imaging campaign and used to remove the artifacts in the scene. The artifacts are no longer visible in the imagery, indicating that the offset is in fact consistent through the imagery. This behaviour can be confirmed by the fact that the artifacts are not detectable within the standard deviation per pixel across the 14 scenes. However, this approach may not always be feasible if the variety is low within the scenes. Additionally, a decrease in artifact-related pixel offset can be observed throughout single imaging campaigns. This can be caused by the recency of the exposure to the Sun. This behaviour has been observable within an the imaging campaign of La Palma conducted on September, 23rd. Here, one of the artifacts within the data has decreased in intensity by approximately 33 % in the 15 minutes between imaging the target and free-space calibration. Due to operational constraints, the free-space calibration prior to imaging the target has been omitted in this imaging campaign. Consequently, the new artifact could not be removed for this particular imaging campaign.

To compare both methods of removing artifacts, they were applied to a sample data set of the United States west coast captured on August, 31st 2021 between 22:42:54 and 22:45:51 UTC. A coastal scene was chosen as reference image. While the mean DN of the corrected frames were almost identical, the median difference between scene-based and dark-frame corrected frames amounted to approximately 22.51 DN with a standard deviation of 115.54 DN. In this example, this amounted to a median difference in brightness temperature of 0.40 K at a standard deviation of 1.97 K. The imaging campaign consisted of a total of 21 individual frames. Consequently, the second approach remains less accurate in reconstructing the original pixel values.

3.3. Application of the wildfire detection algorithm

For the purpose of validating the wildfire detection algorithm, it has been applied to the thermal infrared data retrieved in the experimental imaging campaigns. To this end, the data is first corrected and converted to brightness temperatures on ground. The application of the fire detection algorithm on a sample image is shown in Figures 10 and 11. The TIR scene (Figure 10) features a high number of clouds as well as a small wildfire burning in the center of the image. The wildfire is located in the Western United States and is spread across a line of approximately 8.2 km. The section of the image that contains the wildfire is shown magnified in the top left corner of the image surrounded by clouds. Figure 11 shows the associated cloud and fire map which is the result of the TUBIN fire detection algorithm. Here, white pixels denote clouds, red pixels denote active fires while dark pixels are non-specified background pixels. The algorithm is successful in detecting the hot, active portions of the fire fronts while smaller fires or what appears to be smoldering portions of the wildfires in the image remain undetected. The detection of cloud pixels appears to be very accurate using the determined brightness temperature threshold.

3.4. Detection of other high-temperature events

Within the first months of operating TUBIN, there have been several events of volcanic activity in different areas of the world that are observable from orbit. A total of three different active volcanoes could be imaged by the TIR cameras of TUBIN. The active Etna [32] in Sicily, Italy could be imaged during a campaign conducted on the 3rd of August, 2021. The Cumbre Vieja on La Palma, Spain was successfully targeted during eruptions [33, 34, 35] by TUBIN a total of 5 times between the 21st of September and the 19th of October. A third target was the active Mount Kilauea, Hawaii [36] captured on the 7th and 8th of October, respectively. While the volcanic activity imaged on Sicily and Hawaii was contained within the respective craters, the eruption on La Palma created a stream of lava flowing down the volcano into the ocean. Figure 12 shows a TIR image of a volcanic eruption of the Cumbre Vieja volcano captured by TUBIN.

3.5. Imaging capabilities of the payload assembly

The capabilities of the payload assembly were examined at suitable targets that exhibit fine features such as cities. To this end, an imaging campaign has been conducted with VIS and TIR imagers to capture Las Vegas in the United States. Figure 13 shows the VIS image of the campaign. The city is located on the right-hand side of the frame. The street grid and structures such as the airport are clearly identifiable within the imagery. Figure 14 shows the corresponding scene imaged with one of the microbolometer sensors. Due to the smaller field of view, the city located in the center of the screen covers a larger portion of the frame. The level of detail when compared the VIS image is reduced. However, the localisation of the street grid and the position of large structures such as the airport were still detectable. Lake Mead, for instance, situated at the right-hand side of both images exhibits a high contrast in both scenes.

Another field of interest for the use of VIS data is the observation of light-pollution of cities at night to investigate the capabilities of TUBIN's VIS imager for this

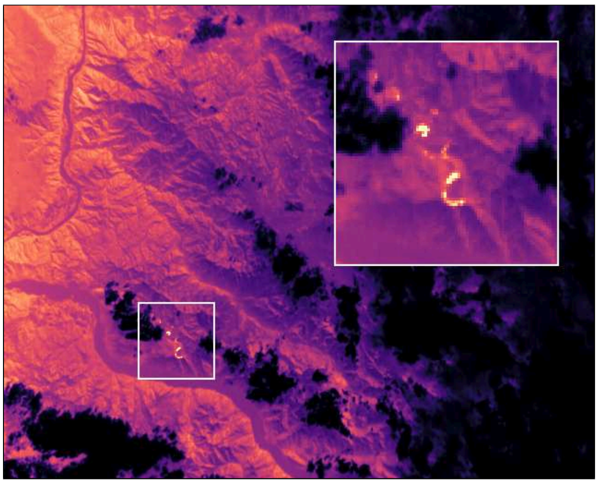

Figure 10: Daytime TIR imagery that contains wildfires taken on August, 31st 2021 at 22:45:51 UTC over the western United States. The region highlighted with a white square is shown in more detail in the upper right corner.

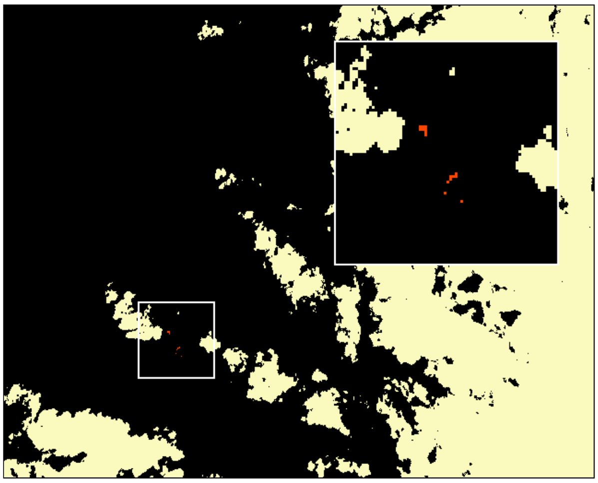

Figure 11: Associated cloud and wildfire mask created from the satellite data using the TUBIN wildfire detection algorithm. Black pixels denote background pixels, white pixels denote cloud pixels and red pixels denote fire pixels. The region highlighted with a white square is shown in more detail in the upper right corner.

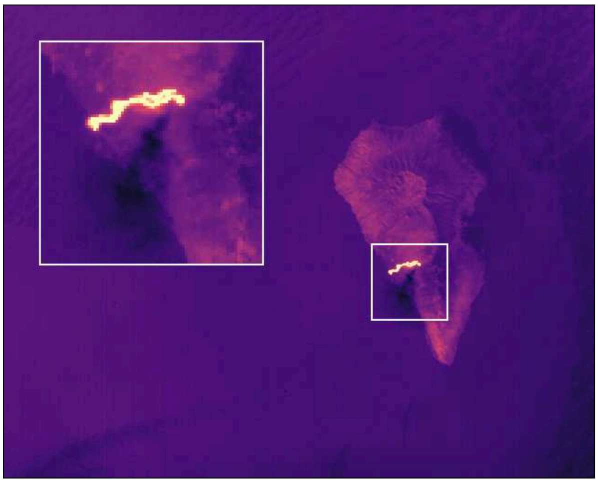

Figure 12: TUBIN TIR scene depicting an eruption of the Cumbre Vieja volcano in La Palma, Spain taken on the on October, 2nd 2021 at 15:27:52 UTC. The scene shows the lava stream from the volcanic crater running into the ocean in bright yellow.

task. A sample image is shown in Figure 15. Again, the street grid and larger structures such as the airport could easily be identified and the location of the main street exhibiting bright light sources was clearly visible. For night time imaging campaigns, the TUBIN TIR camera was used to examine if the target area was obstructed by clouds during image acquisition and, doing so, validated the brightness within the VIS imagery. For the shown image it could be verified that the northern part of Las Vegas was partially obstructed by clouds and, thus, appears darker.

3.6. Payload operations in numbers

During the first six months of operation, TUBIN performed more than 50 dedicated imaging campaigns to examine and verify the capabilities of platform and imaging payload. In total, 820 frames were captured with the microbolometer sensors in 32 imaging campaigns and 654 scenes were captured with the VIS imager within 43 imaging campaigns predominantly in full resolution (3664 x 2748, 39 m GSD) or in reduced resolution (912 x 688, 155 m). The imaging campaigns had various purposes that can roughly be subdivided into detection of high-temperature events, measurement of light-pollution, assessment of attitude determination and control parameters, as well as general testing and calibration campaigns. 124 scenes taken in 15 campaigns with the microbolometer sensors within this time frame featured high-temperature events (64 scenes featured wildfires and 62 images featured volcanic activities). Furthermore, 384 frames featured clouds and 179 were taken for calibration purposes. Seven campaigns imaging cities at night were conducted with the VIS camera assisted by the TIR cameras that provided imagery to estimate the degree of cloud coverage. In total, more than 2 GB of payload data was downlinked in the first six months of mission operations.

4. Discussion and Outlook

Within the first six months of operations, TUBIN captured a substantial number of wildfires and other high-temperature events in a total of 15 imaging campaigns. It could be shown that the raw sensor data exhibited artifacts caused by direct exposure to the Sun. Here, the calibration by subtracting dark frames captured during free-space pointing before and after the acquisition of payload data proved successful in correcting the data. Furthermore, a second less accurate approach to removing the artifacts from the imagery was successfully applied to data sets lacking calibration frames. The detection of wildfires proved successful even for data that was processed using this scene-based correction.

The application of the fire detection algorithm developed on the basis of simulated TUBIN data derived from ASTER and TET-1 imagery proved successful for sample imagery. While a statistical analysis is yet to be conducted, the results are promising. On the sample images shown in Figures 10 and 11 the major active fire fronts are successfully detected while dimmer areas of the fire front, covering a smaller percentile of the pixel area or smoldering portions of the fire remain undetected. In all examined examples across the TIR data, no false-positive was detected which highlights the reliability of detected high-temperature events.

To improve the quality of the collected payload data, the thermal infrared cameras shall be re-calibrated in-orbit to validate the sensor response. This validation can be performed by vicarious calibration using lakes, monitored areas in the ocean, gas flares, or lunar imagery [37, 38]. Gas flares, for instance, constitute small, hot targets that can be used to radiometrically and geometrically calibrate the TIR imagers [25]. Additionally, a cross-calibration campaign with another satellite providing data in the thermal infrared range of the electromagnetic spectrum is envisaged. Potential candidates for this campaign are currently being evaluated.

Having validated the sensor response, the fire detection algorithm shall be re-evaluated and refined using gathered data of wildfires and high-temperature events. Improved thresholds will result in higher detection rates. Another focus going forward is the creation of a data product comprised of registered TIR and VIS

Figure 13: Day time VIS image of Las Vegas in the United States taken on August, 8th 2021 at 22:07:26 UTC.

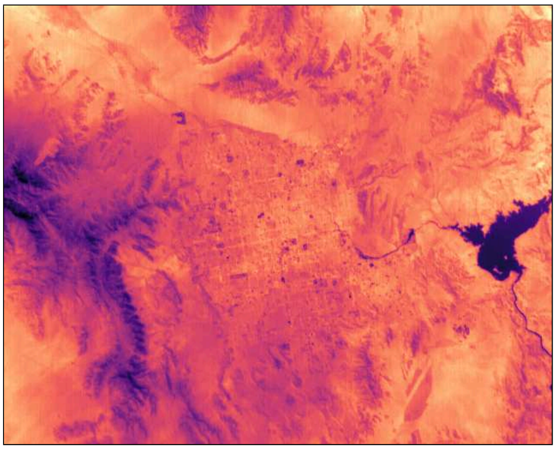

Figure 14: Day time TIR image of Las Vegas in the United States taken on August, 8th 2021 at 22:07:24 UTC.

Figure 15: TUBIN night time VIS image of Las Vegas in the United States taken on November, 2nd 2021 at 09:23:16 UTC.

imagery. There were a high-number of detectable common features within the imagery as shown in Figures 13 and 14. This will improve the cloud detection and, thus, aid in the detection of wildfires.

The operational scheme for detecting wildfires of researching high-temperature events and manually commanding the spacecraft to collect data at the determined location proved the suitability of microbolometers for these tasks. However, this approach requires a significant amount of manual commanding of the satellite and does not enable the detection of wildfires formerly unknown to the operator. In the future, the spacecraft shall be enabled to detect wildfires autonomously. This generates requirements on both payload-side and platform-side. Up to now, the TIR imagery was exclusively preprocessed, converted to brightness temperatures, and examined for high-temperature events on ground. For autonomous operations, the spacecraft is required to perform these steps in-orbit and, thus, needs to:

1. Organize calibration and target data
2. Apply the closest master correction frame
3. Convert raw data to brightness temperature data
4. Apply improved cloud detection with VIS data (optional)
5. Apply the TUBIN fire detection algorithm
6. Isolate the locations of wildfires in the imagery

On the platform's side, the requirements for automated operations revolve around the execution of different tasks depending on the position of the spacecraft on its orbit. The area of interest for fire detection are landmasses below certain latitudes depending on season. The spacecraft shall autonomously determine when it passes an area of interest by propagating its orbit and initiate the calibration procedure before and after collecting imagery in nadir pointing. If the spacecraft is passing a ground station with an exploitable elevation it shall autonomously transmit captured fire data. Furthermore, the time between payload operations shall be used for processing the gathered data. The first steps of satellite platform automation were already implemented and tested in orbit. TUBIN can predict future passes over ground stations and configure the spacecraft to prepare for data downlink. Within the pass, target pointing towards the ground station is performed and the spacecraft is reconfigured to the nominal operational mode afterwards. A second automation mode was implemented for payload imaging at specific times or specific locations. Here, the spacecraft autonomously performs the acquisition of payload data of the target and free-space for calibration. Further updates of the platform automation are envisaged in the future.

In comparison to the TIR imagers, the TUBIN VIS imager exhibits a higher resolution which aids in georeferencing of the imaging data. Furthermore, the VIS imager shall be used to estimate the mounting matrices of the payload assembly with respect to the star trackers by imaging constellations of stars or other celestial bodies. Another field of application is the examination of light-pollution at night using the VIS imager. Here, the TIR imagers could successfully be used to validate whether the cities were obstructed by clouds since they do not require solar irradiation to detect clouds.

5. Conclusion

The TUBIN spacecraft, launched in late June 2021, successfully completed its first six months in orbit. It constitutes the second instalment of the TUBiX20 platform of the chair of space technology at Technische Universität Berlin, a modular microsatellite platform to support missions of up to approximately 50 kg. Tasked with the detection of wildfires using microbolometer technology, TUBIN verified its capabilities within the first two weeks in which wildfires could be detected in TIR imagery of Brasil captured by the spacecraft. In the following weeks and months, more imaging campaigns were conducted and more than 120 images containing high-temperature events could be captured. A portion of these images contained readings of volcanic activities, as well, demonstrating that microbolometers sensitive in the thermal-infrared range of the electromagnetic spectrum are generally suitable for such tasks. It was shown that the TIR imagers suffered from artifacts introduced by direct irradiation by the Sun which could successfully be corrected for. Examining the TIR and VIS imagery, common features were detectable which enables registering TIR and VIS imagery as a prerequisite for georeferencing. Registered data in both spectral ranges also assists the cloud detection fidelity of the system. Moreover, the TUBIN spacecraft has been used to examine light-pollution of cities at night. Within the second half of the mission, the payload assembly shall be calibrated and the fire detection algorithm shall be updated with the gathered wildfire data. These upgrades constitute the prerequisites of an envisaged automated fire identification with TUBIN. To this end, the detection of wildfires shall be conducted on-orbit within an automated operational scheme by the spacecraft.

Acknowledgements

The TUBIN mission and the XLink IOD project are funded by the Federal Ministry for Economic Affairs and Energy (BMWi) through the German Aerospace Center (DLR) on the basis of a decision of the German Bundestag (Grant No. 50 RM 1102 and 50 YB 2009).

References

[1] C. P. Morice, J. J. Kennedy, N. A. Rayner, J. Winn, E. Hogan, R. Killick, R. Dunn, T. Osborn, P. Jones, I. Simpson, An updated assessment of near-surface temperature change from 1850: The HadCRUT5 data set, Journal of Geophysical Research: Atmospheres 126 (3) (2020).

[2] D. Coumou, S. Rahmstorf, A decade of weather extremes, Nature climate change 2 (7) (2012) 491–496.

[3] D. M. Bowman, C. A. Kolden, J. T. Abatzoglou, F. H. Johnston, G. R. van der Werf, M. Flannigan, Vegetation fires in the anthropocene, Nature Reviews Earth & Environment 1 (10) (2020) 500–515.

[4] J. Bartholomäus, M. F. Barschke, M. Lehmann, The TUBIN mission within the context of present and future satellite-based fire detection systems, in: Proceedings of the 12th IAA Symposium on Small Satellites for Earth Observation, Berlin, Germany, 2019.

[5] R. S. Allison, J. M. Johnston, G. Craig, S. Jennings, Airborne optical and thermal remote sensing for wildfire detection and monitoring, Sensors 16 (8) (2016) 1310.

[6] G. Furano, G. Meoni, A. Dunne, D. Moloney, V. Ferlet-Cavrois, A. Tavoularis, J. Byrne, L. Buckley, M. Psarakis, K.-O. Voss, et al., Towards the use of artificial intelligence on the edge in space systems: Challenges and opportunities, IEEE Aerospace and Electronic Systems Magazine 35 (12) (2020) 44–56.

[7] M. F. Barschke, C. Jonglez, P. Werner, P. von Keiser, K. Gordon, M. Starke, M. Lehmann, Initial orbit results from the TUBiX20 platform, Acta Astronautica 167 (2020) 108–116.

[8] K. Gordon, M. F. Barschke, P. Werner, From TechnoSat to TUBIN: performance upgrade for the TUBiX20 microsatellite platform based on flight experience, CEAS Space Journal (2020) 1–11.

[9] M. von der Ohe, S. Weiß, S. Kapitola, L. Gratton, TU Berlin satellite programmatics and multi-ground station concept, in: Proceedings of the 2nd IAA Latin American Symposium on Small Satellites, Buenos Aires, Argentina, 2019.

[10] D. Költzsch, M. F. Barschke, Finite element analysis aided structure design for a modular nanosatellite platform, in: Proceedings of the 11th IAA Symposium on Small Satellites for Earth Observation, 2017, pp. 351–354.

[11] J. Kühn, M. F. Barschke, D. Költzsch, Development of a thermal simulation tool for nanosatellites based on commercial finite element analysis software, in: Proceedings of the 11th IAA Symposium on Small Satellites for Earth Observation, Berlin, Germany, 2017, pp. 385–388.

[12] C. Jonglez, K. Gordon, P. Werner, J. Bartholomäus, M. F. Barschke, ADCS performance assessment using payload camera: lessons learned on a small satellite mission and future applications, in: Proceedings of the 16th International Conference on Space Operations, Online, 2021.

[13] M. Starke, M. F. Barschke, P. von Keiser, A modular hardware diagnosis framework for small spacecraft, in: Proceedings of the 69th International Astronautical Congress, Bremen, Germany, 2018.

[14] P. Werner, M. Starke, A. Graf, K. Gordon, M. F. Barschke, Modular electrical ground support equipment for nanosatellites, in: Proceedings of the 10th IAA Symposium on Small Satellites for Earth Observation, Berlin, Germany, 2015.

[15] L. Giglio, I. Csiszar, Á. Restás, J. T. Morisette, W. Schroeder, D. Morton, C. O. Justice, Active fire detection and characterization with the advanced spaceborne thermal emission and reflection radiometer (ASTER), Remote sensing of environment 112 (6) (2008) 3055–3063.

[16] M. F. Barschke, J. Bartholomäus, K. Gordon, M. Lehmann, K. Brieß, The TUBIN mission for wildfire detection using nanosatellites, CEAS Space Journal 9 (2017) 183–194.

[17] J. Bartholomäus, C. Jonglez, P. von Keiser, J. Léglise, M. Lehmann, P. Werner, M. Barschke, M. Reibe, K. Jäckel, A last-minute upgrade: Rapid integration of an opportunity payload into the TUBIN mission, in: Proceedings of the 36th Annual Small Satellite Conference, Logan, Utah, USA, 2020.

[18] M. F. Barschke, K. Gordon, A generic systems architecture for a single-failure tolerant nanosatellite platform, in: Proceedings of the 64th International Astronautical Congress, Toronto, Canada, 2014.

[19] C. Jonglez, M. F. Barschke, J. Bartholomäus, P. Werner, ADCS performance assessment using payload camera: Lessons learned on a small satellite mission and future applications, in: Proceedings of the 16th International Conference on Space Operations, Cape Town, South Africa, 2021.

[20] J. Bennie, T. W. Davies, J. P. Duffy, R. Inger, K. J. Gaston, Contrasting trends in light pollution across europe based on satellite observed night time lights, Scientific reports 4 (1) (2014) 1–6.

[21] P. Han, J. Huang, R. Li, L. Wang, Y. Hu, J. Wang, W. Huang, Monitoring trends in light pollution in China based on nighttime satellite imagery, Remote Sensing 6 (6) (2014) 5541–5558.

[22] M. Abrams, The advanced spaceborne thermal emission and reflection radiometer (aster): Data products for the high spatial resolution imager on nasa's terra platform, International Journal of Remote Sensing 21 (5) (2000) 847–859.

[23] E. Lorenz, S. Mitchell, T. Säuberlich, C. Paproth, W. Halle, O. Frauenberger, Remote sensing of high temperature events by the firebird mission, The International Archives of Photogrammetry, Remote Sensing and Spatial Information Sciences 40 (7) (2015) 461–467.

[24] J. Bartholomäus, M. F. Barschke, M. Lehmann, Development of a single-channel wildfire detection algorithm for the TUBIN mission, in: Proceedings of the 69th International Astronautical Congress, Bremen, Germany, 2018.

[25] A. Soszynska, Parametrisation of gas flares using FireBIRD infrared satellite imagery, Ph.D. thesis, Humboldt-Universität zu Berlin (2021).

[26] C. D. Elvidge, D. Ziskin, K. E. Baugh, B. T. Tuttle, T. Ghosh, D. W. Pack, E. H. Erwin, M. Zhizhin, A fifteen year record of global natural gas flaring derived from satellite data, Energies 2 (3) (2009) 595–622.

[27] M. Blackett, Review of the utility of infrared remote sensing for detecting and monitoring volcanic activity with the case study of shortwave infrared data for Lascar volcano from 2001–2005, Geological Society, London, Special Publications 380 (1) (2013) 107–135.

[28] L. Giglio, W. Schroeder, C. O. Justice, The collection 6 MODIS active fire detection algorithm and fire products, Remote Sensing of Environment 178 (2016) 31–41.

[29] W. Schroeder, P. Oliva, L. Giglio, I. A. Csiszar, The new VIIRS 375 m active fire detection data product: Algorithm description and initial assessment, Remote Sensing of Environment 143 (2014) 85–96.

[30] C. Cao, X. Xiong, R. Wolfe, F. De Luccia, Q. Liu, S. Blonski, G. Lin, M. Nishihama, D. Pogorzala, H. Oudrari, et al., Visible infrared imaging radiometer suite (VIIRS) sensor data record (SDR) users guide, NOAA Technical Report NESDIS: College Park, MD, USA (2013).

[31] D. A. Dorn, O. Herrera, C. Tesdahl, E. Shumard, Y.-W. Wang, Impacts and mitigation strategies of sun exposure on uncooled microbolometer image sensors, in: Infrared Technology and Applications XXXVII, Vol. 8012, SPIE, 2011, pp. 1279–1288.

[32] G. V. Program, Report on Etna (Italy), weekly volcanic activity report, 4 august - 10 august 2021, Smithsonian Institution and US Geological Survey (2021).

[33] G. V. Program, Report on La Palma (Spain), weekly volcanic activity report, 29 september - 5 october 2021, Smithsonian Institution and US Geological Survey (2021).

[34] G. V. Program, Report on La Palma (Spain), weekly volcanic activity report, 6 october - 12 october 2021, Smithsonian Institution and US Geological Survey (2021).

[35] G. V. Program, Report on La Palma (Spain), weekly volcanic activity report, 13 october - 19 october 2021, Smithsonian Institution and US Geological Survey (2021).

[36] G. V. Program, Report on Kilauea (United States), weekly volcanic activity report, 6 october - 12 october 2021, Smithsonian Institution and US Geological Survey (2021).

[37] J. R. Schott, S. J. Hook, J. A. Barsi, B. L. Markham, J. Miller, F. P. Padula, N. G. Raqueno, Thermal infrared radiometric calibration of the entire Landsat 4, 5, and 7 archive (1982–2010), Remote Sensing of Environment 122 (2012) 41–49.

[38] T. Kouyama, S. Kato, M. Kikuchi, F. Sakuma, A. Miura, T. Tachikawa, S. Tsuchida, K. Obata, R. Nakamura, Lunar calibration for ASTER VNIR and TIR with observations of the Moon in 2003 and 2017, Remote Sensing 11 (22) (2019) 2712.